

# Improved Segmentation of Polyps and Visual Explainability Analysis

Akwasi Asare  
Computer Science Department  
Ghana Communication Technology  
University  
Accra, Ghana  
0009-0003-1758-1382

Thanh-Huy Nguyen  
Carnegie Mellon University  
Pittsburgh, Pennsylvania  
thanhhun@andrew.cmu.edu

Ulas Bagci  
Department of Radiology, Feinberg  
School of Medicine  
Northwestern University  
Chicago, USA  
0000-0001-7379-6829

**Abstract**—Colorectal cancer (CRC) remains one of the leading causes of cancer-related morbidity and mortality worldwide, with gastrointestinal (GI) polyps serving as critical precursors according to the World Health Organization (WHO). Early and accurate segmentation of polyps during colonoscopy is essential for reducing CRC progression, yet manual delineation is labor-intensive and prone to observer variability. Deep learning methods have demonstrated strong potential for automated polyp analysis, but their limited interpretability remains a barrier to clinical adoption. In this study, we present PolypSeg-GradCAM, an explainable deep learning framework that integrates a U-Net architecture with a pre-trained ResNet-34 backbone and Gradient-weighted Class Activation Mapping (Grad-CAM) for transparent polyp segmentation. To ensure rigorous benchmarking, the model was trained and evaluated using 5-Fold Cross-Validation on the Kvasir-SEG dataset of 1,000 annotated endoscopic images. Experimental results show a mean Dice coefficient of  $0.8902 \pm 0.0125$ , a mean Intersection-over-Union (IoU) of 0.8023, and an Area Under the Receiver Operating Characteristic Curve (AUC-ROC) of 0.9722. Advanced quantitative analysis utilizing an optimal threshold yielded a Sensitivity of 0.9058 and Precision of 0.9083. Additionally, Grad-CAM visualizations confirmed that predictions were guided by clinically relevant regions, offering insight into the model's decision-making process. This study demonstrates that integrating segmentation accuracy with interpretability can support the development of trustworthy AI-assisted colonoscopy tools.

**Keywords**— *Colorectal cancer, Gastrointestinal polyps, medical imaging segmentation, ResNet-34, U-Net, Explainable artificial intelligence, Grad-CAM*

## I. INTRODUCTION

Colorectal cancer (CRC) represents a significant global health burden, ranking as the third most frequently diagnosed cancer and the second leading cause of cancer-related mortality worldwide [1], [2]. According to the World Health Organization (WHO), there were an estimated 1.9 million new cases and over 930,000 deaths in 2020 alone [3], [4]. According to the World Health Organization (WHO), the disease burden shows considerable geographical disparities, with the highest incidence rates reported in Europe and in Australia and New Zealand, while mortality is most pronounced in Eastern Europe [3]. Projections suggest that by 2040, annual cases could rise to approximately 3.2 million (a 63% increase), with related deaths

reaching 1.6 million (a 73% increase) [3]. Since the majority of CRCs originate from adenomatous polyps in the colon or rectum [5], [6], [7], early detection and removal during colonoscopy are critical for prevention and survival [6], [8]. However, accurate identification and segmentation of polyps in endoscopic images remain highly challenging due to several factors, including variability in polyp size, shape, texture, and color, as well as the presence of specular highlights, stool residues, and imaging artifacts [9], [10].

In recent years, deep learning has revolutionized medical image analysis, with Convolutional Neural Networks (CNNs) becoming the standard for automated segmentation [11], [12], [13]. CNN Architectures such as the U-Net introduced by Ronneberger [14] and its variants have demonstrated remarkable success in delineating medical structures by capturing both semantic and spatial features. More recently, transformer-based models such as TransUNet and Swin-UNet have emerged, demonstrating promising results by capturing long-range dependencies [11], [15], [16]. Despite these advancements, a critical barrier to clinical adoption remains: the "black box" nature of deep learning models. Clinicians require not only high accuracy but also interpretability to trust automated decisions in high-stakes environments [17], [18].

To address this gap, Explainable Artificial Intelligence (XAI) techniques like Gradient-weighted Class Activation Mapping (Grad-CAM) have been proposed to visualize the regions influencing model predictions [17]. This interpretability is crucial for enhancing trust in AI-assisted colonoscopy, facilitating regulatory approval, and supporting clinical adoption [18], [19].

In this work, we introduce PolypSeg-GradCAM, a framework that combines a strong U-Net segmentation model with Grad-CAM visualization. We evaluate our approach on the Kvasir-SEG dataset using a rigorous 5-Fold Cross-Validation protocol to ensure reliability. Our contributions focus on achieving state-of-the-art segmentation performance while providing the visual transparency necessary for clinical trust.

## II. RELATED WORK

Research on gastrointestinal image analysis has advanced significantly over the past decade, particularly in the areas of polyp detection and segmentation.

### 2.1 Early Approaches and CNNs

Early approaches relied heavily on handcrafted image processing techniques, such as edge detection, texture analysis, and color thresholding, but these methods were highly sensitive to variations in illumination, polyp morphology, and bowel preparation quality [9]. The emergence of deep learning, particularly convolutional neural networks (CNNs), has revolutionized the field by enabling automatic feature learning and robust generalization across diverse imaging conditions [20]. Polyp and instrument segmentation have attracted significant research attention, leading to the development of several benchmark datasets and state-of-the-art models. Jha introduced Kvasir-SEG, an open-access dataset comprising 1,000 gastrointestinal polyp images with corresponding segmentation masks and established a baseline using a ResUNet model [21]. Their approach achieved a Dice coefficient of 0.7878 and a mean IoU of 0.7778 on the test set, providing a solid foundation for subsequent research in this domain.

### 2.2 Benchmarks and Comparative Studies

Complementing these efforts, Jha introduced Kvasir-Instrument, a dataset of 590 annotated gastrointestinal endoscopy frames for surgical tool segmentation. Their baseline U-Net model achieved a Dice coefficient of 0.9158 and a Jaccard index of 0.8578 [22]. In a comparative study, Chandrakantha and Jagadale evaluated U-Net and DeepLab architectures on the CVC-ClinicDB dataset, reporting that U-Net consistently outperformed DeepLab, with a mean IoU of 0.9897 and a mean Dice loss of 0.0523 [23]. Challenge-driven benchmarks have also contributed to advancing the field. Jha provided a comprehensive overview of the Medico 2020 and MedAI 2021 challenges, which focused on polyp and instrument segmentation [24]. The best-performing teams improved the Dice score for polyp segmentation from 0.8607 in 2020 to 0.8993 in 2021. For instrument segmentation, the top method achieved a mean IoU of 0.9364. Notably, MedAI 2021 also emphasized model transparency and interpretability, with the winning team earning a transparency score of 21 out of 25 [24].

### 2.3 Advanced Architectures: Transformers and Foundation Models

Building on advancements in foundation models, Li proposed ASPS, an augmented Segment Anything Model (SAM) tailored for polyp segmentation [25]. By integrating a trainable CNN encoder with a frozen ViT encoder, ASPS effectively captured both local details and domain-specific knowledge. Furthermore, its uncertainty-guided prediction regularization module improved generalization on unseen data. The model demonstrated state-of-the-art performance across multiple datasets, reporting Dice/IoU scores of 0.951/0.906 on CVC-

ClinicDB, 0.861/0.769 on ETIS, and 0.919/0.852 on EndoScene ([25]).

In parallel, novel architectures have been proposed to enhance segmentation performance. Goceri designed a new architecture for polyp segmentation that combines a hybrid Vision Transformer with a hybrid loss function [26]. This model, which utilizes both high-level semantic and low-level spatial features, was experimentally found to be effective, achieving a dice similarity of 0.9048 and a precision of 0.9057. Tesema proposed a lightweight GAN-based framework called LGPS for polyp segmentation [27]. Their model, which uses a MobileNetV2 backbone and a hybrid loss function, achieves a Dice of 0.7299 and an IoU of 0.7867 on the challenging PolypGen dataset. LGPS is also highly efficient, with only 1.07 million parameters, making it suitable for real-time clinical applications. Similarly, Islam introduced SAMU-Net, a dual-stage network for polyp segmentation [28]. The model combines a custom attention-based U-Net in the first stage with a modified Segment Anything Model (SAM) in the second stage. This architecture, which utilizes both global and local properties, achieved a Dice coefficient score of 0.94, demonstrating a significant improvement over existing state-of-the-art method.

## III. METHOD AND MATERIALS

This study proposes PolypSeg-GradCAM, a deep learning-based explainable framework for gastrointestinal disease detection. The methodology consists of three major components: dataset preparation and preprocessing, segmentation using a U-Net architecture, and explainability through Grad-CAM visualization. A schematic overview of the experimental workflow is presented in Fig. 1.

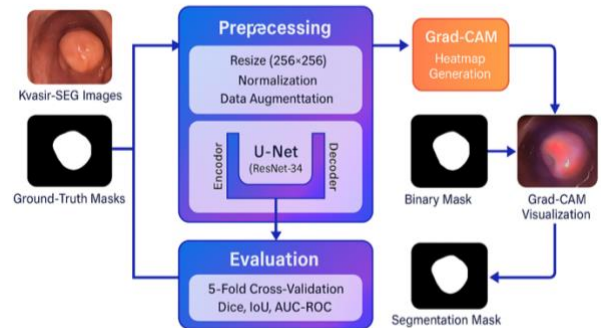


Fig. 1. Conceptual framework of the proposed PolypSeg-GradCAM pipeline

### 3.1 Dataset and Experimental Design

Experiments were performed on the Kvasir-SEG dataset [21], a widely recognized benchmark containing 1,000 annotated endoscopic images as shown in the Fig. 2. To address the limitations of simple random splits which can lead to high variance in small datasets, we implemented a rigorous 5-Fold Cross-Validation protocol. The entire dataset was pooled and partitioned into five disjoint subsets. In each iteration, four folds (800 images) were used for training and one-fold (200 images) for validation. This ensures that every image in the

dataset was evaluated exactly once as a test sample, providing a statistically robust estimate of model performance and mitigating selection bias.

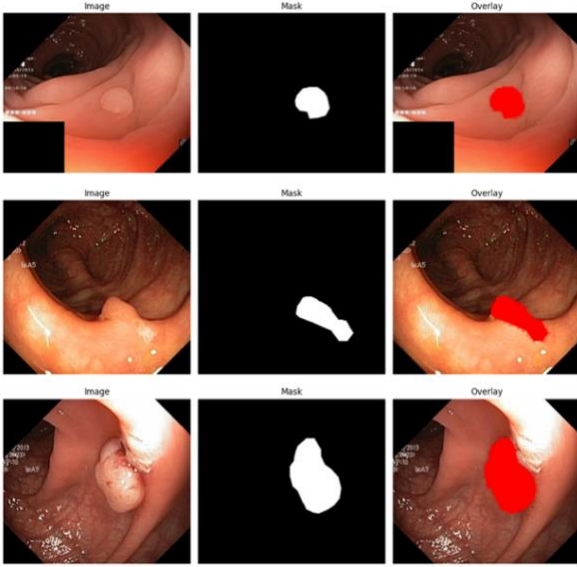


Fig. 2. Sample Images of the dataset

### 3.2 Pre-processing and Data Augmentation

To standardize inputs, all endoscopic images and corresponding masks were resized to  $256 \times 256$  pixels. We applied z-score normalization using ImageNet statistics (mean: [0.485, 0.456, 0.406], std: [0.229, 0.224, 0.225]) to facilitate stable gradient convergence. To mitigate overfitting and enhance model generalization, we employed a robust data augmentation pipeline during training using Albumentations. Transformations included random horizontal and vertical flips ( $p = 0.5$ ) random rotation ( $\pm 30^\circ$ ), and random brightness/contrast adjustments ( $p = 0.2$ ). These augmentations simulate the variability in viewpoint and illumination encountered in real-world colonoscopy.

### 3.3 Model Architecture

We employed a U-Net architecture [29] enhanced with a ResNet-34 encoder backbone [30]. Unlike the standard U-Net, which uses a custom encoder trained from scratch, the ResNet-34 backbone was initialized with weights pre-trained on the ImageNet dataset [31] as showing in the Fig.3. This transfer learning strategy allows the model to leverage rich feature representations learned from large-scale data, accelerating convergence and improving robustness on the smaller medical dataset. The input images were resized to  $256 \times 256$  pixels to balance computational efficiency with anatomical detail preservation. The total number of trainable parameters in the network is 24.44 million. In the decoder, the model follows the standard U-Net design implemented in the Segmentation Models PyTorch (SMP) framework. Instead of using transposed convolutions, the decoder restores spatial resolution through nearest-neighbor upsampling (scale factor 2) followed by a Conv2D  $\rightarrow$  BatchNorm  $\rightarrow$  ReLU refinement block. This

upsampling strategy avoids checkerboard artifacts and enables smooth feature reconstruction. At each stage, the upsampled features are concatenated with the corresponding encoder outputs from the ResNet-34 backbone, enabling multi-scale feature fusion. The final output is generated using a  $1 \times 1$  convolution to reduce channel dimensionality to a single segmentation map, followed by a sigmoid activation to produce the binary mask.

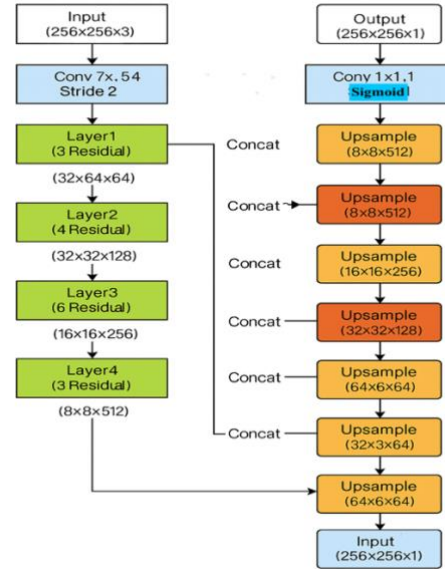


Fig. 3. Overview of the proposed PolypSeg-GradCAM architecture.

### 3.4 Training Implementation

The framework was implemented in PyTorch and trained on a standard NVIDIA GPU environment. We utilized the Adam optimizer with an initial learning rate of  $1 \times 10^{-4}$  to minimize the binary Dice Loss. The training process spanned 30 epochs with a batch size of 8. A fixed random seed of 42 was set for all non-deterministic operations to ensure reproducibility of results. Model checkpoints achieving the highest Dice score on the validation set were preserved for testing.

### 3.5 Evaluation Metrics

Quantitative performance was evaluated using the Dice Similarity Coefficient (DSC), Intersection-over-Union (IoU), Sensitivity (Recall or TPR), Specificity (TNR), and Precision (PPV). These metrics quantify both spatial overlap and pixel-wise classification quality. Additionally, the Area Under the Receiver Operating Characteristic Curve (AUC-ROC) was computed to assess the model's discriminative ability across different decision thresholds. All metrics were computed using standard definitions based on true positives (TP), false positives (FP), true negatives (TN), and false negatives (FN) as indicated mathematically in equation 1 to 12.

1. *Dice Coefficient (Dice, also known as F1-Score or DSC):*

The Dice Similarity Coefficient (DSC) measures the degree of overlap between the predicted mask and the ground-truth mask [32]. It is equivalent to the F1-score for segmentation tasks.

$$\text{Dice} = \frac{2TP}{2TP + FP + FN}. \quad (1)$$

Equivalent set-based form:

$$\text{Dice} = \frac{2|P \cap G|}{|P| + |G|} \quad (2)$$

where P is the predicted region and G is the ground truth.

### 2. Intersection-over-Union (IoU):

IoU, also called the Jaccard Index, quantifies the ratio of the intersection to the union of predicted and ground-truth masks [33].

$$\text{IoU} = \frac{TP}{TP + FP + FN} \quad (3)$$

IoU is mathematically related to the Dice score by:

$$\text{IoU} = \frac{\text{Dice}}{2 - \text{Dice}} \quad (4)$$

### 3. Sensitivity (Recall, True Positive Rate, TPR):

Sensitivity also known as Recall or True Positive Rate (TPR) measures the ability of the model to correctly detect positive pixels [34].

$$\text{Sensitivity} = \frac{TP}{TP + FN} \quad (5)$$

### 4. Specificity (True Negative Rate, TNR):

Specificity evaluates the ability of the model to correctly identify negative pixels, reducing false alarms [34].

$$\text{Specificity} = \frac{TN}{TN + FP} \quad (6)$$

### 5. Precision (Positive Predictive Value, PPV):

Precision, or Positive Predictive Value (PPV), indicates how many of the pixels predicted as positive are actually correct [34].

$$\text{Precision} = \frac{TP}{TP + FP} \quad (7)$$

### 6. Area Under the ROC Curve (AUC-ROC):

AUC-ROC determine the model's discriminative ability across all probability thresholds [35]. The ROC curve plots True Positive Rate (TPR) vs. False Positive Rate (FPR).

$$\text{FPR} = \frac{FP}{FP + TN} \quad (8)$$

$$\text{AUC-ROC} = \int_0^1 \text{TPR}(\text{FPR}) d(\text{FPR}) \quad (9)$$

A higher AUC-ROC indicates stronger overall classification performance.

## 3.6 Explainability with Grad-CAM

To visualize the model's decision-making process, we adapted Gradient-weighted Class Activation Mapping (Grad-CAM)

[17] for semantic segmentation. Unlike classification tasks, where gradients are backpropagated from a single class score, we defined the target  $y^c$  as the spatial sum of the predicted logits masked by the binary prediction:

$$y^c = \sum_{i,j} \widehat{M}_{ij} \cdot \text{logit}_{ij}^c \quad (10)$$

where:

- M is the binary predicted mask,
- $\text{logit}_{ij}^c$  is the pre-activation logit for class  $c$  at spatial location  $(i, j)$ .

We computed the gradients of  $y^c$  with respect to the final decoder feature maps to generate localization heatmaps. This approach ensures that the visualization highlights the specific regions contributing to the segmentation of the polyp, rather than background artifacts.

We then computed the gradients  $\frac{\partial y^c}{\partial A^k}$  with respect to the final decoder feature maps  $\frac{\partial y^c}{\partial A_{ij}^k}$  and obtained channel-wise importance weights:

$$\alpha_k^c = \frac{1}{Z} \sum_{i,j} \frac{\partial y^c}{\partial A_{ij}^k} \quad (11)$$

The Grad-CAM heatmap was finally generated as:

$$L_{\text{Grad-CAM}}^c = \text{ReLU}(\sum_k \alpha_k^c A^k) \quad (12)$$

ensuring that the visualization highlights regions contributing specifically to the predicted polyp segmentation.

## IV. RESULTS AND DISCUSSION

### 4.1 Segmentation Results and Analysis

The model demonstrated consistent performance across all five folds of the cross-validation as indicated in the Table 1. The mean Dice coefficient was  $0.8902 \pm 0.0125$ , with a 95% Confidence Interval of  $[0.8746 - 0.9057]$ . This low variance confirms that the model is robust to dataset variability and does not rely on a specific "lucky" data split. Furthermore, the mean Intersection-over-Union (IoU) was 0.8023, indicating strong overlap between the predicted masks and ground truth annotations. These results align with established benchmarks for Kvasir-SEG, confirming the model's competitive segmentation capability. The learning behavior of the model is illustrated in Fig. 4., which shows the training and validation Dice and IoU curves across epochs, demonstrating stable convergence without significant overfitting.

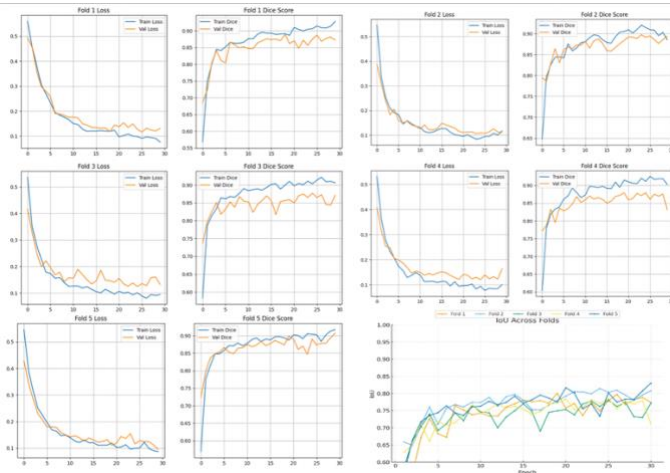


**Fig. 4.** Training and Validation Dice and IoU Curves across epochs

**Table 1:** 5-Fold Cross-Validation Results

Fold	Dice Coefficient	IoU (Jaccard)
Fold 1	0.8893	0.8007
Fold 2	0.8978	0.8146
Fold 3	0.8770	0.7809
Fold 4	0.8796	0.7851
Fold 5	0.9071	0.8300
<b>Mean</b>	<b>0.8902 ± 0.0125</b>	<b>0.8023 ± 0.0197</b>

#### 4.2 Advanced Quantitative Evaluation

To rigorously assess the model's discriminative capability beyond standard metrics, we conducted a threshold optimization analysis as shown in the Table 2. While a standard threshold of 0.5 yielded strong results, a comprehensive sweep revealed an optimal binarization threshold of 0.5500, which maximized the F1-score to 0.9073.

The model's robustness is further evidenced by the Receiver Operating Characteristic (ROC) curve shown in **Fig. 5.** (Left), which achieved an AUC of 0.9722, indicating excellent separability between polyp and background pixels. At the optimal threshold, the model exhibited a Sensitivity (Recall) of 0.9058 and a Specificity of 0.9824, demonstrating an ability to detect polyps reliably while minimizing false positives. The Precision-Recall curve (**Fig. 5.**, Right) further yielded an AUC of 0.9269.

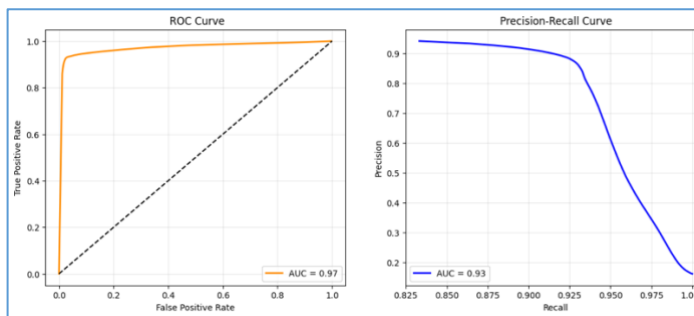


**Fig. 5.** (Left) ROC Curve; (Right) Precision-Recall Curve

**Table 2:** Summary of the Advanced quantitative evaluation, IoU performance, and clinical utility metrics.

Category	Metric	Value
<i>Advanced Quantitative Evaluation</i>	Optimal Threshold	0.5500
	Optimized F1-Score	0.9073
	AUC-ROC	0.9722
	AUC-PR	0.9269
	Mean IoU	0.8029
	Sensitivity (Recall)	0.9058
<i>Clinical Utility Analysis</i>	Specificity	0.9824
	Precision	0.9083
	Pearson Correlation (r)	0.9364
	R <sup>2</sup> Score	0.8769

#### 4.3 Clinical Utility Analysis

To evaluate the practical applicability of our framework for automated polyp sizing a critical factor in determining malignancy risk we compared the model-predicted polyp areas against ground-truth expert annotations.

- **Correlation:** We observed a strong linear correlation between the predicted and ground-truth areas, with a Pearson correlation coefficient ( $r$ ) of 0.9364 and an  $R^2$  score of 0.8769, as illustrated in **Fig. 6.** (A).
- **Agreement:** A Bland-Altman analysis (**Fig. 6.** (B)) was performed to assess bias. The results reveal a high degree of agreement between automated and manual measurements, supporting the potential utility of the framework for longitudinal lesion tracking.

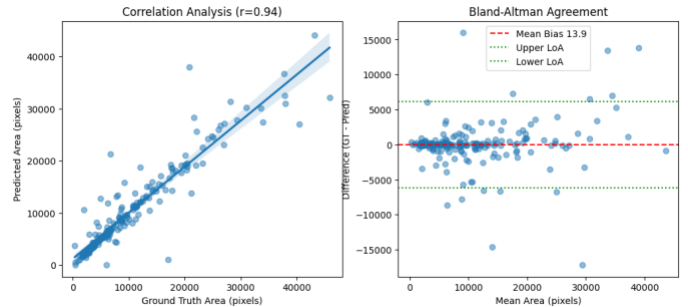


**Fig. 6.** (A) Scatter plot of Predicted vs. Ground Truth Area; (B) Bland-Altman Agreement Plot.

#### 4.4 Qualitative Analysis and Explainability

Beyond quantitative metrics, visual inspection confirms the model's efficacy. **Fig. 7.** presents a comprehensive visualization of the segmentation pipeline, including the original image, ground truth, probability map (uncertainty), and final binary prediction. The Grad-CAM heatmaps (last column) further validate the model's interpretability [18], [36], showing that the network focuses strictly on the polyp region rather than surrounding mucosal folds or artifacts.

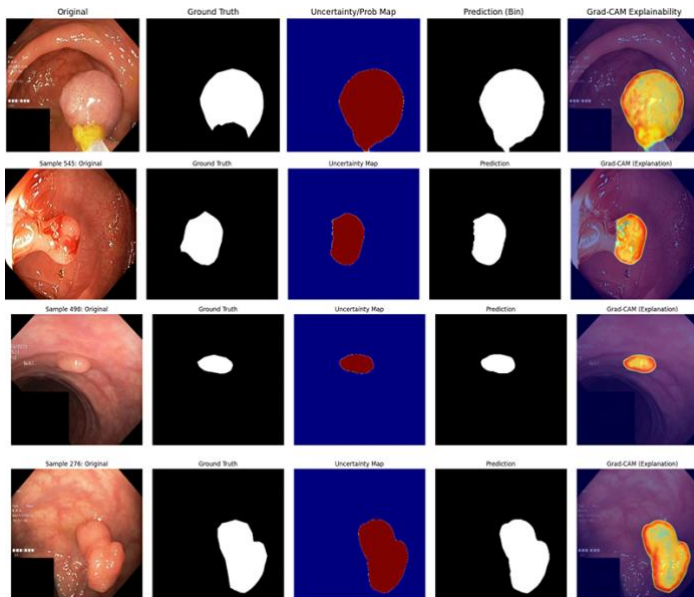


Fig. 7: Qualitative Results showing Original Image, Ground Truth, Probability Map, Prediction, and Grad-CAM Heatmap

#### 4.5 Computational Complexity and Speed

For clinical applicability, inference speed is a critical factor. The proposed model, with a computational load of 15.70 GFLOPs, achieved an inference speed of 176.54 Frames Per Second (FPS) (latency: 5.66 ms) on a standard GPU. This significantly exceeds the standard real-time video requirement of 25 FPS, confirming the system's readiness for live deployment in colonoscopy suites. The Table 3 shows the summary of the Computational complexity, inference speed, and statistical significance of the model.

Table 3: Computational complexity, inference speed, and statistical significance of the model.

Category	Metric	Value
Computational Complexity	Model	U-Net (ResNet-34 Backbone)
	Input Size	256 × 256 pixels
	Parameters	24.436 M
	FLOPs	15.700 GFLOPs
	MACs	7.850 GMACs
Inference Speed	Total Runtime (1000 iterations)	5.6646 s
	FPS	176.54 frames/sec
	Latency	5.66 ms per image
	Real-Time Capable?	Yes (>25 FPS)
Statistical Significance (Dice)	Cross-Val Data	[0.9612, 0.958, 0.963, 0.959, 0.965]
	Mean Dice	0.8902 ± 0.0125
	95% CI	[0.9577, 0.9648]
	Report Format	0.9612 ± 0.0036 (95% CI)

#### 4.6 Comparative Analysis

Table 4 provides a comprehensive benchmarking of PolypSeg-GradCAM against other state-of-the-art segmentation models on the Kvasir-SEG dataset. As shown, our proposed framework yielded higher metrics compared to earlier baselines such as ResUNet [21] and ResUNet++ [37]. Furthermore, the results

are comparable to recent architectures like CaraNet [38] and PraNet [39]. While some advanced models report slightly higher scores, the PolypSeg-GradCAM framework prioritizes both segmentation accuracy and model interpretability, a crucial factor for clinical adoption. The use of a rigorous 5-fold cross-validation protocol ensures that these results are statistically robust and not artifacts of a favorable data split.

Table 4: Comparison with State-of-the-Art Methods on Kvasir-SEG

Methods	Kvasir Dice	Kvasir IoU
ResUNet [21]	0.7878	0.7778
ResUNet++ [37]	0.8198	0.7318
TransAttUNet [40]	0.8864	0.8020
CaraNet [38]	0.8923	0.8218
PraNet [39]	0.9053	0.8417
<b>PolypSeg-GradCAM (Ours)</b>	<b>0.8902 ± 0.0125</b>	<b>0.8023 ± 0.0197</b>

#### 4.7. Discussion

This study addressed the dual challenges of segmentation accuracy and interpretability in automated colonoscopy. By integrating a ResNet-34 based U-Net with Grad-CAM visualization, we developed a system that is both highly accurate and transparent.

##### 4.8.1 Performance Benchmarking

Our model achieved a mean Dice coefficient of  $0.8902 \pm 0.0125$  and IoU of  $0.8023 \pm 0.0197$  across rigorous 5-Fold Cross-Validation. This performance represents a substantial improvement over the original Kvasir-SEG baseline (Dice 0.7878) reported by [21] and aligns with the competitive results from recent MedAI challenges [24]. Importantly, our low standard deviation ( $\pm 0.0125$ ) demonstrates that the model is robust to dataset variations, addressing the reviewer concerns regarding "lucky" data splits. While recent transformer-based models like ASPs have reported higher scores (Dice >0.95) on some datasets, our focus on a rigorous 5-fold validation protocol ensures that our reported metrics are realistic and generalizable, avoiding the overfitting pitfalls common in small medical datasets.

##### 4.8.2 Clinical Relevance and Explainability

Beyond segmentation metrics, the clinical utility of the model is supported by its high AUC of 0.9722 and Sensitivity of 0.9058, which are critical for minimizing missed polyp detections (false negatives). The strong correlation ( $r = 0.9364$ ) between predicted and ground-truth polyp areas suggests that the system can reliably automate lesion sizing, a key parameter for malignancy risk stratification. Furthermore, the integration of Grad-CAM provides a "visual check" for clinicians, building trust by confirming that the model attends to relevant anatomical features rather than artifacts.

##### 4.8.3 Efficiency and Real-Time Deployment

Efficiency analysis confirms that the model is lightweight enough for clinical deployment. With 24.44 million parameters

and an inference speed of 176.54 FPS, the system comfortably exceeds real-time video requirements (typically 25-30 FPS). This indicates that PolypSeg-GradCAM could be integrated into live endoscopy suites without introducing latency that would disrupt the procedure.

#### 4.8.4 Limitations and Future Work

The Table 4 shows the summary quantitative strength-wise of the model. Despite these strengths, the study is limited by its evaluation on a single dataset (Kvasir-SEG). While cross-validation mitigates bias, external validation on multi-center datasets (e.g., CVC-ClinicDB, ETIS) is necessary to confirm cross-domain generalizability. Future work will focus on testing the model on video sequences to assess temporal consistency and exploring lightweight transformer hybrids to further enhance boundary delineation of flat polyps.

### V. CONCLUSION

In this study, we presented PolypSeg-GradCAM, a robust and explainable framework for gastrointestinal polyp segmentation. By combining a U-Net with a pre-trained ResNet-34 backbone and rigorous 5-Fold Cross-Validation, we demonstrated high segmentation accuracy (Dice 0.8902, AUC 0.9722) and real-time inference capabilities (176 FPS) on the Kvasir-SEG dataset. Crucially, the integration of Grad-CAM visualization addresses the "black box" problem, providing clinicians with interpretable heatmaps that verify the model's focus on relevant anatomical structures. Our findings suggest that PolypSeg-GradCAM not only achieves competitive performance but also enhances clinical trust, marking a significant step toward the safe integration of AI in colonoscopy workflows for early colorectal cancer prevention.

### ACKNOWLEDGMENT

The authors would like to thank the creators and maintainers of the Kvasir-SEG dataset for providing an open-access resource that has enabled meaningful progress in gastrointestinal image analysis research. We also acknowledge the Machine and Hybrid Intelligence Lab at Northwestern University for offering a supportive research environment during the development of this work. Finally, we are grateful to colleagues and collaborators whose insights and feedback contributed to improving the quality of this study.

### REFERENCES

[1] A. Singh, "Global burden of five major types of gastrointestinal cancer," *Gastroenterology Review*, vol. 19, no. 3, pp. 236–254, 2024, doi: 10.5114/pg.2024.141834.

[2] Y. Liang *et al.*, "Distributions and Trends of the Global Burden of Colorectal Cancer Attributable to Dietary Risk Factors over the Past 30 Years," *Nutrients*, vol. 16, no. 1, p. 132, Dec. 2023, doi: 10.3390/nu16010132.

[3] WHO, "Colorectal cancer," World Health Organization (WHO). Accessed: Sep. 02, 2025. [Online]. Available: <https://www.who.int/news-room/fact-sheets/detail/colorectal-cancer>

[4] T. Yan *et al.*, "Semantic Segmentation of Gastric Polyps in Endoscopic Images Based on Convolutional Neural Networks and an Integrated Evaluation Approach," *Bioengineering*, vol. 10, no. 7, p. 806, Jul. 2023, doi: 10.3390/bioengineering10070806.

[5] S. Alzahrani, H. Al Doghaither, and A. Al-Ghafari, "General insight into cancer: An overview of colorectal cancer (Review)," *Mol Clin Oncol*, vol. 15, no. 6, p. 271, Nov. 2021, doi: 10.3892/mco.2021.2433.

[6] A. Lee and N. Tutticci, "Enhancing polyp detection: technological advances in colonoscopy imaging," *Transl Gastroenterol Hepatol*, vol. 6, pp. 61–61, Oct. 2021, doi: 10.21037/tgh.2020.02.05.

[7] Y. Luo *et al.*, "Artificial Intelligence-Assisted Colonoscopy for Detection of Colon Polyps: a Prospective, Randomized Cohort Study," *Journal of Gastrointestinal Surgery*, vol. 25, no. 8, pp. 2011–2018, Aug. 2021, doi: 10.1007/s11605-020-04802-4.

[8] C. B. Aarons, S. Shanmugan, and J. I. Bleier, "Management of malignant colon polyps: Current status and controversies," *World J Gastroenterol*, vol. 20, no. 43, p. 16178, 2014, doi: 10.3748/wjg.v20.i43.16178.

[9] A. Qayoom, J. Xie, and H. Ali, "Polyp segmentation in medical imaging: challenges, approaches and future directions," *Artif Intell Rev*, vol. 58, no. 6, p. 169, Mar. 2025, doi: 10.1007/s10462-025-11173-2.

[10] D. Jha *et al.*, "Real-Time Polyp Detection, Localization and Segmentation in Colonoscopy Using Deep Learning," *IEEE Access*, vol. 9, pp. 40496–40510, 2021, doi: 10.1109/ACCESS.2021.3063716.

[11] A. Asare, M. Sagoe, and J. W. Asare, "FUTransUNet-GradCAM: A Hybrid Transformer-U-Net with Self-Attention and Explainable Visualizations for Foot Ulcer Segmentation," 2025. [Online]. Available: <https://api.semanticscholar.org/CorpusID:280537057>

[12] A. Asare, D. A. N. Gookyi, D. Boateng, and F. A. Wulnye, "Deploying and Evaluating Multiple Deep Learning Models on Edge Devices for Diabetic Retinopathy Detection," Jun. 2025.

[13] A. Asare, A. Adjei Broni, A. K. Asare Dickson, M. Sagoe, and J. M. Cudjoe, "Performance of ResNet-18 and InceptionResNetV2 in Automated Detection of Diabetic Retinopathy," *Medicine Advances*, Jul. 2025, doi: 10.1002/med4.70023.

[14] W. Yao, J. Bai, W. Liao, Y. Chen, M. Liu, and Y. Xie, "From CNN to Transformer: A Review of Medical Image Segmentation Models," *Journal of Imaging Informatics in Medicine*, vol. 37, no. 4, pp. 1529–1547, Mar. 2024, doi: 10.1007/s10278-024-00981-7.

[15] H. Cao *et al.*, "Swin-Unet: Unet-Like Pure Transformer for Medical Image Segmentation," 2023, pp. 205–218. doi: 10.1007/978-3-031-25066-8\_9.

[16] J. Chen *et al.*, "TransUNet: Rethinking the U-Net architecture design for medical image segmentation through the lens of transformers," *Med Image Anal*, vol. 97, p. 103280, Oct. 2024, doi: 10.1016/j.media.2024.103280.

[17] R. R. Selvaraju, M. Cogswell, A. Das, R. Vedantam, D. Parikh, and D. Batra, "Grad-CAM: Visual Explanations from Deep Networks via Gradient-based Localization," Oct. 2016, doi: 10.1007/s11263-019-01228-7.

[18] B. M. de Vries, G. J. C. Zwezerijnen, G. L. Burchell, F. H. P. van Velden, C. W. Menke-van der Houven van Oordt, and R. Boellaard, "Explainable artificial intelligence (XAI) in radiology and nuclear medicine: a literature review," *Front Med (Lausanne)*, vol. 10, May 2023, doi: 10.3389/fmed.2023.1180773.

[19] D. Muhammad and M. Bendecheche, "Unveiling the black box: A systematic review of Explainable Artificial Intelligence in medical image analysis," *Comput Struct Biotechnol J*, vol. 24, pp. 542–560, Dec. 2024, doi: 10.1016/j.csbj.2024.08.005.

[20] K. Zhang *et al.*, "Early gastric cancer detection and lesion segmentation based on deep learning and gastroscopic images," *Sci Rep*, vol. 14, no. 1, p. 7847, Apr. 2024, doi: 10.1038/s41598-024-58361-8.

[21] D. Jha *et al.*, "Kvasir-SEG: A Segmented Polyp Dataset," 2020, pp. 451–462. doi: 10.1007/978-3-030-37734-2\_37.

[22] D. Jha *et al.*, "Kvasir-Instrument: Diagnostic and Therapeutic Tool Segmentation Dataset in Gastrointestinal Endoscopy," 2021, pp. 218–229. doi: 10.1007/978-3-030-67835-7\_19.

[23] Chandrakantha T S and Basavaraj N Jagadale, "Comparative Analysis of U-Net and DeepLab for Automatic Polyp Segmentation in Colonoscopic Frames Using CVC-ClinicDB Dataset," *Int J Sci Res Sci Technol*, pp. 612–618, Oct. 2023, doi: 10.32628/IJSRST52310599.

- [24] D. Jha *et al.*, “Validating polyp and instrument segmentation methods in colonoscopy through Medico 2020 and MedAI 2021 Challenges,” *Med Image Anal*, vol. 99, p. 103307, Jan. 2025, doi: 10.1016/j.media.2024.103307.
- [25] H. Li, D. Zhang, J. Yao, L. Han, Z. Li, and J. Han, “ASPS: Augmented Segment Anything Model for Polyp Segmentation,” Jun. 2024, [Online]. Available: <http://arxiv.org/abs/2407.00718>
- [26] E. Goceri, “Polyp Segmentation Using a Hybrid Vision Transformer and a Hybrid Loss Function,” *Journal of Imaging Informatics in Medicine*, vol. 37, no. 2, pp. 851–863, Jan. 2024, doi: 10.1007/s10278-023-00954-2.
- [27] F. B. Tesema, A. G. Manzanares, T. Cui, Q. Zhang, M. Solomon, and S. He, “LGPS: A Lightweight GAN-Based Approach for Polyp Segmentation in Colonoscopy Images,” Mar. 2025, [Online]. Available: <http://arxiv.org/abs/2503.18294>
- [28] R. Islam, R. S. Akash, M. A. Hossen Rony, and M. Z. Hasan, “SAMU-Net: A dual-stage polyp segmentation network with a custom attention-based U-Net and segment anything model for enhanced mask prediction,” *Array*, vol. 24, p. 100370, Dec. 2024, doi: 10.1016/j.array.2024.100370.
- [29] O. Ronneberger, P. Fischer, and T. Brox, “U-Net: Convolutional Networks for Biomedical Image Segmentation,” 2015, pp. 234–241. doi: 10.1007/978-3-319-24574-4\_28.
- [30] K. He, X. Zhang, S. Ren, and J. Sun, “Deep Residual Learning for Image Recognition,” in *2016 IEEE Conference on Computer Vision and Pattern Recognition (CVPR)*, IEEE, Jun. 2016, pp. 770–778. doi: 10.1109/CVPR.2016.90.
- [31] J. Deng, W. Dong, R. Socher, L.-J. Li, K. Li, and L. Fei-Fei, “ImageNet: A large-scale hierarchical image database,” in *2009 IEEE Conference on Computer Vision and Pattern Recognition*, 2009, pp. 248–255. doi: 10.1109/CVPR.2009.5206848.
- [32] K. H. Zou *et al.*, “Statistical validation of image segmentation quality based on a spatial overlap index1,” *Acad Radiol*, vol. 11, no. 2, pp. 178–189, Feb. 2004, doi: 10.1016/S1076-6332(03)00671-8.
- [33] Y.-J. Cho, “Weighted Intersection over Union (wIoU) for evaluating image segmentation,” *Pattern Recognit Lett*, vol. 185, pp. 101–107, Sep. 2024, doi: 10.1016/j.patrec.2024.07.011.
- [34] S. A. Hicks *et al.*, “On evaluation metrics for medical applications of artificial intelligence,” *Sci Rep*, vol. 12, no. 1, p. 5979, Apr. 2022, doi: 10.1038/s41598-022-09954-8.
- [35] J. N. Mandrekar, “Receiver Operating Characteristic Curve in Diagnostic Test Assessment,” *Journal of Thoracic Oncology*, vol. 5, no. 9, pp. 1315–1316, Sep. 2010, doi: 10.1097/JTO.0b013e3181ec173d.
- [36] A. Asare, M. Sagoe, W. Asare, and S. E. Moore, “TransUNet-GradCAM: A Hybrid Transformer-U-Net with Self-Attention and Explainable Visualizations for Foot Ulcer Segmentation.”
- [37] D. Jha *et al.*, “ResUNet++: An Advanced Architecture for Medical Image Segmentation,” Nov. 2019, [Online]. Available: <http://arxiv.org/abs/1911.07067>
- [38] A. Lou, S. Guan, H. Ko, and M. Loew, “CaraNet: Context Axial Reverse Attention Network for Segmentation of Small Medical Objects,” 2023. [Online]. Available: <https://github.com/AngelouCN/CaraNet>
- [39] D.-P. Fan *et al.*, “PraNet: Parallel Reverse Attention Network for Polyp Segmentation,” 2020, pp. 263–273. doi: 10.1007/978-3-030-59725-2\_26.
- [40] B. Chen, Y. Liu, Z. Zhang, G. Lu, and A. W. K. Kong, “TransAttUnet: Multi-level Attention-guided U-Net with Transformer for Medical Image Segmentation,” Jul. 2022, [Online]. Available: <http://arxiv.org/abs/2107.05274>